

## Effect of Argon with Different Oxygen Contents on the Preparation of Rare-Earth Steel Powders by Electrode-Induced Gas Atomization

**Authors:** Wang, Prof. Qian, Li, Miss Ji, Qi, Mr. Zijun, Hu, Prof. Xiaoqiang, Prof. Hao Lan, Chen, Prof. Yi, Wei, Dr. Qi, Dr. Qi Wei

**Date:** 2025-12-01T20:41:20+00:00

### Abstract

In this paper, three groups of Fe-Cr-Ti-Y alloy powders were prepared by Electrode-induced gas atomization (EIGA) technology using different argon-oxygen mixtures as the atomization medium. Through characterization of the solidification structure combined with thermodynamic and kinetic analysis, the effects of oxygen content and powder particle size on the oxidation behaviors of the powders were investigated. The results show that the element concentration gradient and its differential binding affinity with oxygen jointly drive the formation of the surface oxide layer during droplet solidification. As the oxygen content increases from 0.5 vol.% to 1.0 vol.%, the oxidation mechanism transitions from internal chromium diffusion to combined thermodynamic and diffusion-kinetic control. The surface structure evolved from a Fe-rich oxide layer to a Cr-rich one. When the oxygen content was 0.5 vol.% and the powder particle size exceeded 110  $\mu\text{m}$ , oxide layer delamination was not pronounced. In this case, the Y element was significantly segregated at the oxide layer/matrix interface.

### Full Text

## Effect of Argon with Different Oxygen Contents on the Preparation of Rare-Earth Steel Powders by Electrode-Induced Gas Atomization

Qian Wang<sup>1,2</sup>, Ji Li<sup>1,2</sup>, Zijun Qi<sup>3</sup>, Xiaoqiang Hu<sup>2,4</sup>, Hao Lan<sup>2</sup>, Yi Chen<sup>3</sup>, Qi Wei<sup>2</sup>,

<sup>1</sup> School of Chemistry and Materials Science, University of Science and Technology of China, Hefei 230026, China

<sup>2</sup> Key Laboratory of Rare Earths, Ganjiang Innovation Academy, Chinese Academy of Sciences, Ganzhou 341000, China

<sup>3</sup> School of Materials Science and Engineering, Nanchang Hangkong University, Nanchang 330063, China

<sup>4</sup> Shenyang National Laboratory of Materials Science, Institute of Metal Research, Chinese Academy of Sciences, Shenyang 110016, China

**Abstract:** In this study, three groups of Fe-Cr-Ti-Y alloy powders were prepared by electrode-induced gas atomization (EIGA) using argon-oxygen mixtures with varying oxygen concentrations as the atomization medium. By characterizing the solidification structure and conducting thermodynamic and kinetic analyses, we investigated the effects of oxygen content and powder particle size on the oxidation behavior of the powders.

The results demonstrate that the formation of the surface oxide layer during droplet solidification is driven by the combined influence of elemental concentration gradients and differences in oxygen binding affinity. As oxygen content increases from 0.5 vol.% to 1.0 vol.%, the oxidation mechanism transitions from chromium internal diffusion to combined thermodynamic and diffusion kinetic control, accompanied by an evolution of the surface structure from a Fe-rich oxide layer to a Cr-rich one. At an oxygen content of 0.5 vol.% with powder particle sizes exceeding 110 nm, oxide layer delamination was not pronounced, and significant segregation of Y occurred at the oxide layer/matrix interface.

**Keywords:** Electrode-induced gas atomization; Powder particle size; Oxidation behaviors; Thermodynamics; Kinetics

---

## 1. Introduction

The operating temperature, irradiation dose, and corrosive environment in fourth-generation nuclear energy systems are substantially more severe than in previous generations, imposing higher performance requirements on structural materials [?]. Oxide dispersion-strengthened (ODS) steel has attracted considerable attention for these applications [?, ?]. The key principle involves introducing highly stable nano-oxide dispersions into the matrix, which effectively pin dislocations and grain boundaries [?], thereby significantly improving creep resistance and radiation tolerance.

Traditional ODS steels produced by mechanical alloying suffer from drawbacks including process complexity, susceptibility to impurity contamination, inferior powder morphology, and poor batch-to-batch reproducibility, which limit their large-scale application [?, ?]. Atomizing molten steel with argon-oxygen gas mixtures shows promising potential for simplifying the process and improving powder quality [?]. The underlying mechanism is that a metastable surface oxide layer serves as an oxygen source [?], providing oxygen that promotes formation of Y-Ti-O nanophases during subsequent hot isostatic pressing [?].

This novel approach has spurred extensive follow-up research to further explore the innovative process. Rieken et al. [?] pioneered the successful preparation of ODS ferritic alloy powders by vacuum induction melting gas atomization (VIGA) using an argon-oxygen gas mixture. However, VIGA exhibits inherent limitations, primarily its reliance on crucibles that cause unavoidable melt contamination [?, ?]. Furthermore, continuous high-temperature melting exacerbates chromium evaporation, presenting considerable challenges for precise compositional control [?]. Consequently, VIGA cannot satisfactorily produce high-purity ODS steel powders.

Therefore, alternative atomization routes must be evaluated to fundamentally address these VIGA-related issues. After reviewing available technologies, we identified electrode-induced gas atomization (EIGA) as the most promising process for detailed investigation, precluding exhaustive experimental study of all techniques. Besides VIGA, widely used technologies for producing high-performance metal powders include EIGA, plasma rotating electrode process (PREP), plasma atomization (PA), ultrasonic gas atomization (USGA), and electron beam rotating atomization (EBRA), each exhibiting distinct characteristics regarding powder purity, morphology, material applicability, and economic cost. Specifically, PREP and EBRA can produce high-purity powders with excellent sphericity, but stringent requirements for machinable electrodes and low yields of fine powders limit their application in research and large-scale production [?, ?]. While PA can achieve high-purity powders with flexible raw material forms, it suffers from relatively low productivity and high operating costs [?]. As an enhanced VIGA variant, USGA improves powder size distribution and morphology but fails to overcome fundamental ceramic contamination issues, making it unsuitable for our research system [?].

In comprehensive comparison, the EIGA process emerges as a feasible alternative for manufacturing reactive and oxygen-sensitive alloys, yielding high-quality powders [?]. Renowned for its crucible-free operation and localized melting with rapid droplet detachment, EIGA effectively eliminates contamination, minimizes elemental evaporation and oxygen adsorption, and produces high-purity titanium-based and nickel-based superalloy powders with low oxygen content [?, ?]. However, EIGA's application for fabricating ODS steel powders remains largely unexplored. To address this gap, we prepared powders by EIGA using different argon-oxygen mixtures as the atomization medium and characterized the metastable oxide layer on powder surfaces, focusing specifically on how its thickness, composition, and structure depend on two critical variables: oxygen content and particle size. Based on these results, we aim to establish a novel foundation and define a viable process window for fabricating high-performance ODS steels via oxygen-doped argon gas atomization of molten steel.

## 2.1 Materials and Methods

Powder preparation was conducted at Asia New Materials (Beijing) Co., Ltd., where three batches of ODS steel powders were produced by EIGA. We systematically investigated the effects of different oxygen contents (0.1 vol.%, 0.5 vol.%, and 1.0 vol.% O<sub>2</sub>) in the atomizing gas on powder characteristics. The parent alloy electrode was a Fe-15Cr-0.1Ti-0.7Y (wt.%) bar measuring 50 mm in diameter and 600 mm in length. During atomization, the induction melting current was set to 42 A, the electrode rotation speed was maintained at 20 rad/s, and the atomization pressure was set to 4 MPa. Prior to atomization, the atomization chamber was evacuated to a vacuum of 10<sup>-3</sup> Pa, after which argon-oxygen mixed gas with different oxygen doping ratios was introduced as the atomization medium. Powder samples were collected after preparation.

---

## 2.2 Powder Characterization

The obtained powders were sieved, and three particle size ranges (<53 μm, 53–100 μm, and 100–280 μm) were selected for characterization. Metallic element concentrations were determined by inductively coupled plasma mass spectrometry (ICP-MS). Powder surface morphologies were examined by scanning electron microscopy (SEM) and dual-beam focused ion beam microscopy (FIB-SEM), with simultaneous acquisition of secondary electron (SE) and backscattered electron (BSE) images. Chemical composition distribution on surfaces was analyzed using the equipped energy-dispersive X-ray spectrometer (EDS) at an accelerating voltage of 10–15 kV. The thickness of oxygen-rich regions in powder cross-sections was measured for different particle sizes and subsequently converted to surface oxide volume fractions to clarify the relationship between particle size and surface oxide volume fraction. Thermodynamic reactions for each alloy phase were calculated using Thermo-Calc 2025a software with the TCFE12 database to obtain oxidation driving forces during melting and solidification. Equilibrium phase fractions as functions of temperature were obtained to clarify dissolution and precipitation behaviors, while thermodynamic driving forces for oxide formation were calculated using HSC 6.0 software.

---

## 3.1 Morphologies of the Oxidized Surfaces

Table 1 presents surface chemical composition analysis of powders prepared under different atomization atmospheres. As the oxygen content in the atomizing gas increased from 0.1 vol.% to 1.0 vol.%, the mass percentage of oxygen on the powder surface correspondingly increased to 9.91 wt.%, 13.21 wt.%, and 16.92 wt.%, respectively. These results demonstrate that atomizing gas oxygen content significantly affects the extent of powder surface oxidation. With increasing oxygen content, concentrations of Fe, Cr, and other major alloying elements fluctuate.

tuated, while enrichment of Y and Ti on the surface became progressively more pronounced.

**Table 1.** Analysis of powder elements obtained by atomization with different oxygen contents.

Fig. 1 [Figure 1: see original paper] shows SEM morphologies of powder surfaces under different oxygen contents. Figs. 1a-c display overall powder morphologies. Powders atomized with 0.1 vol.% O<sub>2</sub> (Fig. 1a) exhibited a narrow particle size distribution, high sphericity, and good flowability. Increasing oxygen content to 0.5 vol.% resulted in a higher proportion of satellite particles and compromised flowability (Fig. 1b). At the highest oxygen content of 1.0 vol.%, morphologies were severely degraded, characterized by irregular particle shapes and a bimodal size distribution (Fig. 1c). Figs. 1d-f illustrate corresponding surface microstructure evolution of individual powder particles. As oxygen content increased from 0.1 vol.% to 0.5 vol.%, surface pits grew noticeably in both dimensions and number density (Figs. 1d-e). At 1.0 vol.% O<sub>2</sub> (Fig. 1f), surfaces developed orange-peel wrinkles and surface roughness increased sharply. Figs. 1g-i show high-magnification surface morphologies, revealing evolution from a continuous three-dimensional reticular structure at 0.1 vol.% O<sub>2</sub> (Fig. 1g), through an equiaxed crystal structure at 0.5 vol.% (Fig. 1h), to orange-peel-like wrinkles with micropores and localized dendritic bulges at 1.0 vol.% O<sub>2</sub> (Fig. 1i). This transition reflects features of non-equilibrium solidification, indicating that solidification interface stability is destroyed as oxygen content increases.

**Fig. 1** SEM morphologies of powder surfaces atomized at oxygen contents of 0.1 vol.%, 0.5 vol.%, and 1.0 vol.% in the atomizing gas: (a-c) macroscopic powder morphologies, (d-f) overall morphologies of individual powder particles, (g-i) local morphologies of individual powder particles.

---

### 3.2 Cross-Sectional Morphologies of Powders

To investigate oxidation behaviors of ODS steel powders under different oxygen contents, powder cross-sections were examined. Figs. 2, 3, and 4 show SEM images and EDS elemental maps of 40 μm powder cross-sections at oxygen contents of 0.1 vol.%, 0.5 vol.%, and 1.0 vol.%, respectively. As shown in Fig. 2 [Figure 2: see original paper], at 0.1 vol.% oxygen, the oxide layer was thin with discontinuous oxygen-deficient regions. At this stage, a kinetic competition occurs: Fe, Cr, and Ti are preferentially oxidized due to rapid diffusion, forming a discontinuous surface layer. Y, with its low diffusivity, is blocked by this surface layer and cannot reach oxygen-deficient regions, resulting in extensive accumulation within the matrix phase beneath the oxide layer.

**Fig. 2** SEM and EDS images of the cross-section of the oxidized surface of a powder particle with oxygen content of 0.1 vol.% and particle size of 40 μm.

Fig. 3 [Figure 3: see original paper] shows that when atomizing gas oxygen content increased to 0.5 vol.%, oxide layer thickness increased with continuous, uniform oxygen distribution. Elemental distribution maps revealed that Fe, Cr, Y, and Ti were all highly enriched in the powder oxide layer. Variations in atomizing gas oxygen content produced discernible differences in metallic oxide distribution within the powder oxide layer. Since Fe diffuses more rapidly than Cr, it preferentially reaches the particle outer surface and reacts with oxygen at limited reactive sites, forming a thin Fe-rich oxide layer. Beneath this layer lies a metallic subsurface depleted in Fe but enriched in Cr. Y formed a continuous oxide film beneath the Cr-rich metallic subsurface, while Ti oxides were dispersed as discontinuous particles of varying sizes.

**Fig. 3** SEM and EDS images of the cross-section of the oxidized surface of a powder particle with oxygen content of 0.5 vol.% and particle size of 40  $\mu\text{m}$ .

Fig. 4 [Figure 4: see original paper] shows that when atomizing gas oxygen content increased to 1.0 vol.%, oxide layer thickness continued to increase. These results demonstrate that increasing oxygen content effectively promotes formation of thicker, more continuous surface oxide layers. High oxygen content provides sufficient reactants for gas-liquid interface reactions and accelerates oxidation kinetics. Cr possesses greater thermodynamic driving force for oxidation than Fe, leading to its selective oxidation. A thin layer predominantly composed of Cr-rich oxides formed on the powder surface, beneath which lay a metallic sublayer depleted in Cr but enriched in Fe.

**Fig. 4** SEM and EDS images of the cross-section of the oxidized surface of a powder particle with oxygen content of 1.0 vol.% and particle size of 40  $\mu\text{m}$ .

In all samples, oxygen was primarily enriched in the powder surface layer, reacting with metallic elements to form oxide layers. Factors influencing the distinct distribution of metallic oxides can be categorized into three aspects. First, for a fixed powder particle size, a strong positive correlation exists between oxygen content and oxide layer thickness. Second, increasing oxygen content from 0.1 vol.% to 1.0 vol.% drives evolution in powder characteristics, where sphericity transitions from poor to optimal and back to poor. Third, surface oxide composition evolves from incomplete coverage through an Fe-rich active layer to a dense Cr-rich barrier. These findings demonstrate that maintaining atomizing gas oxygen content at 0.5 vol.% or below represents the optimal choice, lying precisely within the critical transition zone where oxide layer structure evolves from insufficient to excessive, ensuring both oxide layer integrity and ideal reactivity. Based on this, we further focused on the optimal oxygen content (0.5 vol.%) to investigate variations in surface oxide volume fractions across different powder particle sizes, as discussed in the following section.

### 3.3 Oxide Volume Fractions

With the optimal batch identified, we investigated powder surface oxide volume fraction to establish its correlation with particle size. Powders atomized at 0.5 vol.% oxygen (shown in Fig. 3) were sieved to obtain particles of various sizes. Particles with sizes of 30  $\mu\text{m}$ , 50  $\mu\text{m}$ , 70  $\mu\text{m}$ , 90  $\mu\text{m}$ , 110  $\mu\text{m}$ , 125  $\mu\text{m}$ , 190  $\mu\text{m}$ , 230  $\mu\text{m}$ , and 300  $\mu\text{m}$  were selected to measure oxygen-rich region thickness from elemental maps of powder cross-sections. These measured values were converted to surface oxide volume fractions. Fig. 5 [Figure 5: see original paper] shows that for a fixed atomizing gas oxygen content, the surface oxide volume fraction was lower for coarse particles than for fine particles.

**Fig. 5** Relationship between surface oxide volume fraction and particle size.

This observed trend is linked to the specific surface area of powder particles, a key parameter dictating the resultant oxide volume fraction. Assuming spherical particles, particle volume  $V$  scales with the cube of radius while surface area  $A$  scales with the square of radius. Consequently, the relative proportion of oxide layer in coarse particles becomes markedly diluted due to rapidly expanding particle volume, resulting in substantial decreases in oxide volume fraction. Thus, the specific surface area ( $A/V$  ratio) decreases with increasing particle size. In summary, powder oxidation behavior depends on both atomizing gas oxygen content and particle size. At the optimal oxygen content of 0.5 vol.%, decreasing particle size increases specific surface area, which significantly raises the relative surface oxide content. Both parameters must be considered together to achieve powders with low oxygen content and ideal microstructure.

---

### 4.1 Element Distribution in the Oxide Layer: A Theoretical Model for Droplet Solidification

Fig. 6 [Figure 6: see original paper] presents a thermodynamic model illustrating element distribution within the oxide layer of powders atomized with oxygen-doped inert gas. Fig. 6a tracks oxygen migration paths by monitoring oxygen content evolution in each phase during droplet solidification. The process begins with liquid-phase separation above the liquidus temperature, generating a (Y, Ti, O)-enriched liquid phase for subsequent ultrafine composite oxides. Solidification initiates first in the rapidly cooling outer droplet layer as system temperature approaches the liquidus. Simultaneously, (Fe, Cr) solid solution formation releases oxygen to the surface, where oxidation reactions form (Fe, Cr)<sub>2</sub>O<sub>3</sub> surface oxide films. Uniformly distributed Y and Ti become enriched in the final solidified residual liquid phase. As temperature drops below the liquidus, the solid-liquid interface advances inward, and oxygen and active elements become extremely enriched in the remaining liquid phase. This enrichment facilitates Y-rich oxide formation through conversion of (Fe, Cr)<sub>2</sub>O<sub>3</sub> and direct precipitation from the (Y, Ti, O)-rich liquid. Concurrently, metallic

element combinations generate Laves phases. When temperature falls below the solidus, the liquid phase disappears completely and solidification ends. Sluggish solid-state diffusion leads to kinetic arrest of the microstructure.

**Fig. 6** In atomized powders, oxide distribution is primarily determined by thermodynamic equilibrium and phase transformation driving forces during droplet solidification: (a) oxygen content in each phase, (b) Gibbs free energy of reaction.

Oxygen-doped inert gas atomization involves oxygen dissolution into the melt and subsequent reaction with metallic elements upon rapid cooling, triggering in-situ oxide precipitation. Comparing driving forces for oxygen dissolution and oxide formation is therefore essential for analyzing elemental distribution within the oxide layer. Fig. 6b shows variation of standard Gibbs free energy change ( $\Delta G^0$ ) as a function of temperature. Oxygen behavior in the high-temperature liquid phase is dominated by its dissolution trend, represented by the red line with negative slope. In contrast, oxide formation during mid-to-low temperature solidification is dictated by the Gibbs free energy trend, represented by the black line with positive slope. Intersection of the red and black lines near the melting point indicates that such oxides dissolve above this temperature and later reprecipitate as fine particles during rapid cooling. Therefore, accelerating cooling rate to rapidly solidify droplets below the liquidus temperature presents an effective process control strategy. This approach leverages non-equilibrium characteristics of rapid solidification to kinetically control high-temperature oxygen dissolution and solute redistribution, thereby preventing excessive surface and internal oxidation and ultimately producing high-performance metal powders with low oxygen content.

Fig. 7 [Figure 7: see original paper] compares thermodynamic driving forces for oxidation among Fe, Cr, Y, and Ti, demonstrating not only obvious disparities in oxygen affinity but also a specific hierarchy: Y, Ti, and Cr all possess stronger affinity than Fe, ranked as  $Y > Ti > Cr$ . During atomization, these reactive elements competitively capture oxygen, altering its distribution between the melt and newly formed oxides. Thus, adding Y, Ti, and Cr to pure Fe enhances the overall oxidation driving force of the resultant Fe-15Cr-0.1Ti-0.7Y (wt.%) alloy. Direct evidence includes preferential nucleation of Y-, Ti-, and Cr-rich oxides on powder surfaces during rapid cooling. A second characteristic is formation of a surface Cr-rich oxide layer with an underlying Cr-depleted/Fe-rich metallic sublayer on powder particles, as shown in Fig. 4, experimentally demonstrating the oxidation sequence  $Y > Ti > Cr > Fe$ .

**Fig. 7** Driving forces for oxide formation of metallic elements.

### 4.2.1 Influence of Oxygen Content on the Rate of Oxygen Diffusion in Droplets

At low oxygen content (0.1 vol.%), the oxide layer was discontinuous with a defective structure, and oxidation kinetics were in an inhibited stage. Limited oxygen flux from gas phase to liquid metal surface made the gas-liquid interfacial reaction the rate-limiting step for the overall process. Specifically, interfacial oxygen concentration  $C$  was extremely low, leading to negligible inward chemical potential gradient ( $dC/dx$ ). Consequently, internal oxygen diffusion depth became very shallow, resulting in formation of only a thin oxide film. Additionally, rapid droplet solidification caused volume shrinkage and formation of a solid shell, with resulting stresses tearing the incomplete, poorly bonded oxide film. This non-uniform oxygen distribution is indicative of a kinetically suppressed regime. When oxygen content increased to 0.5 vol.% and 1.0 vol.%, the oxide layer gradually became continuous and dense with significantly increased thickness. The oxidation mechanism transitioned to diffusion control, involving inward diffusion of oxygen ions and outward diffusion of metal cations through the oxide layer. Since both ions exhibit slow diffusion kinetics, they jointly govern the oxidation process.

---

### 4.2.2 Influence of Metallic Element Diffusion on Surface Oxidation

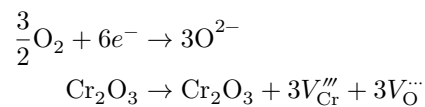
Carl Wagner [?] noted that kinetics of protective oxide formation on alloys are determined by competitive counter-diffusion of oxygen inward and alloying elements outward. Equation (1) describes this competitive relationship, where  $N_O$  is oxygen partial pressure,  $D_O$  is oxygen diffusion coefficient,  $D_M$  is cation diffusion coefficient, and  $N_M$  is the critical concentration of the specific element. Given the low diffusion coefficients of Ti and Y, the oxidation process is dominated by inward oxygen diffusion [?]. Oxygen dissolves into the alloy and reacts with Ti and Y to form internal oxide particles. In contrast, Fe and Cr have larger diffusion coefficients, allowing rapid outward diffusion [?]. A continuous, dense external oxide film enriched in Cr and Fe forms through reaction of Fe and Cr with oxygen at the surface, effectively suppressing subsequent oxidation [?].

Cr migrates through lattice diffusion in iron-based alloys [?]. The lattice diffusion rate is relatively low, and enhancing the chromium diffusion coefficient requires elevated bulk Cr concentration in the alloy. Typically, Cr content must exceed 20 wt.% to form a continuous  $Cr_2O_3$  film [?]. Traditional heat-resistant alloys such as Inconel 600 contain about 15 wt.% Cr, which is insufficient to form a continuous  $Cr_2O_3$  film [?]. However, ODS alloy microstructural design enables a shift in chromium diffusion mechanism by replacing slow lattice diffusion with rapid grain boundary diffusion [?, ?]. Induced by oxygen-doped gas atomization, rapid Cr diffusion during solidification of Fe-15Cr-0.1Ti-0.7Y

(wt.%) droplets thus permits formation of a continuous  $\text{Cr}_2\text{O}_3$  film despite a bulk Cr content of only 15 wt.%.

Fig. 3 shows formation of a thin Fe-rich oxide layer on powder surfaces under 0.5 vol.% oxygen. Beneath this thin layer lies an Fe-poor, Cr-rich metallic subsurface layer. Nyborg [?] confirmed that during atomization of ferritic steel containing 25 wt.% Cr, droplets contacting atomization gas immediately formed a continuous iron oxide layer 3 nm thick. Similar to these results, we found oxidation reaction kinetics were dominant under low oxygen content conditions. Such iron oxide layers are inherent in atomized steel powders. The composition of the initial surface oxide layer, particularly regarding Fe and Cr content, closely mirrors that of the matrix. Subsequent preferential inward diffusion of Cr leads to substitution of Fe atoms within the oxide [?], followed by outward diffusion and further oxidation of displaced Fe to form iron oxides. Concurrently, outward Cr diffusion depletes Cr at the metal/oxide interface, decreasing Cr concentration in the outer portion of the oxide layer. Consequently, the final oxide film exhibits decreasing Cr content from inner to outer regions, complemented by corresponding Fe increase.

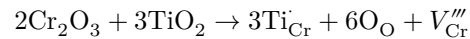
Increasing oxygen content from 0.5 vol.% to 1.0 vol.% fundamentally alters the oxidation mechanism, shifting dominant factors from inward Cr diffusion to combined thermodynamic and kinetic control. Formation of an initial Cr-rich oxide layer depletes local Cr atoms, resulting in relative Fe enrichment. A small amount of  $\text{O}^{2-}$  continues diffusing inward through the Cr-rich oxide layer. Restricted by rapid solidification in gas atomization, timely migration of internal Cr to the surface is hindered. Space charge theory provides an explanation for this process, as shown in equations (2-3) [?]:



Oxygen molecule adsorption and ionization occur at the oxide/gas interface. A positively charged space charge region forms in the near-surface oxide layer due to electron loss to oxygen. To maintain electrical neutrality, chromium vacancies as negatively charged point defects migrate to the surface region. Additionally, inward migration of positively charged point defects leads to formation of an ultrathin space-charge region near the surface with a gradient in point defect concentration.  $\text{Cr}^{3+}$  tends to move toward regions with high chromium vacancy concentration. Since  $D_{\{\text{Cr}\}} \ll D_{\{\text{Fe}\}}$ , the mainstream diffusion path from interior to exterior is blocked [?, ?]. Concurrently,  $\text{O}^{2-}$  diffuses along grain boundaries opposite to chromium vacancy migration, penetrating the initial thin  $\text{Cr}_2\text{O}_3$  layer to reach the  $\text{Cr}_2\text{O}_3$ /metal interface, where it reacts with Fe to form iron oxides. This Fe consumption at the interface disrupts local equilibrium, forcing  $\text{Fe}^{3+}$  from the matrix to diffuse toward the interface. Ultimately, a Cr-poor, Fe-rich metallic subsurface layer forms beneath the Cr-rich oxide thin layer.

This transformation demonstrates that powder oxide layer structure can be precisely regulated by controlling mixed oxygen content, providing an important process basis for preparing oxide dispersion-strengthened alloys with tailored properties.

Internal oxidation behaviors of Y and Ti can also be analyzed from a kinetic perspective. Due to its extremely low solid solubility and small diffusion coefficient, Y cannot diffuse outward rapidly enough to form a continuous Y-rich surface oxide film [?, ?]. Instead, Y segregates via short-circuit diffusion paths such as grain boundaries and phase boundaries [?]. The Y-rich precipitate observed at boundaries is a typical internal oxide that is inert, highly insoluble, and exhibits exceptional thermodynamic stability. As immobile obstacles, these precipitates significantly inhibit outward diffusion of  $\text{Cr}^{3+}$  and  $\text{Fe}^{3+}$ . Ti outward diffusion is slower than O inward diffusion [?], causing Ti enrichment near the growing powder oxide layer, mostly as discontinuous particles. This Ti enrichment characterizes internal oxidation and involves doping of  $\text{Ti}^{4+}$  (with higher valence than  $\text{Cr}^{3+}$ ) into the  $\text{Cr}_2\text{O}_3$  lattice. To maintain electroneutrality, cation vacancies spontaneously generate to compensate for extra positive charge from  $\text{Ti}^{4+}$  dopants. The defect reaction can be expressed as equation (4):



where  $\text{Ti}_{\text{Cr}}^{\cdot\cdot\cdot}$  denotes a Ti atom with effective positive charge on a chromium lattice site, and  $V_{\text{Cr}}^{\prime\prime\prime}$  denotes a cation vacancy with three effective negative charges. These additional cation vacancies provide faster channels or short-circuit paths for outward diffusion of  $\text{Cr}^{3+}$  and  $\text{Fe}^{3+}$  [?].

---

### 4.2.3 Variation of Oxide Layer Type with Powder Particle Size at Constant Oxygen Content

Fig. 8 [Figure 8: see original paper] shows powders atomized with 0.5 vol.% oxygen, revealing a direct correlation between particle size and oxide layer type. A distinct layered structure existed on 40  $\mu\text{m}$  powder particles (Fig. 3). In contrast, 110  $\mu\text{m}$  powder particles displayed a mixed Fe-Cr oxide layer on their outer surface without significant elemental composition variation across the oxide layer.

**Fig. 8** SEM and EDS images of the cross-section of the oxidized surface of a powder particle with oxygen content of 0.5 vol.% and particle size of 110  $\mu\text{m}$ .

This phenomenon can be explained from two perspectives: elemental diffusion kinetics and oxygen penetration depth. Fine particles exhibit higher specific surface area and greater cooling rates, resulting in significantly shortened diffusion paths from particle interior to surface [?]. Consequently, kinetic factors become

the dominant controlling mechanism. Following atomization, preferential occupation of surface active sites by Fe atoms and their reaction with minor  $O_2$  to form iron oxides depletes surface Fe, creating an inward concentration gradient from the powder surface. This concentration gradient drives oxygen inward diffusion. When inward-diffusing oxygen meets outward-diffusing Cr atoms, the relatively slow diffusion rate of Cr predominates. A thin Fe-rich oxide layer forms on the powder surface with an underlying sublayer depleted in Fe and enriched in Cr. Thermodynamically, a portion of initially formed iron oxides can undergo solid-state reduction reaction with chromium, simultaneously yielding a more stable Cr-rich oxide layer that facilitates formation of a continuous, dense chromium oxide barrier.

When particle size increases to 110  $\mu\text{m}$ , the path for elemental outward diffusion is significantly prolonged, making it difficult for Fe to quickly and completely cover the entire surface. Meanwhile, oxygen inward diffusion depth is limited, the oxide layer remains thin, and oxidation reactions are confined to near-surface regions [?]. The spatial conditions required for a distinct oxidation interface cannot be met, and Fe and Cr react with oxygen almost simultaneously, resulting in formation of a mixed Fe-Cr oxide rather than discrete single-metal oxide layers.

---

### 4.3 Y Distribution near the Oxide Layer versus Powder Particle Size

Distinct Y segregation was observed at the oxide/matrix interface in coarse particles. This Y segregation is not an isolated phenomenon but is closely coupled with and mutually promoted by the initial oxidation reaction. Fig. 9 [Figure 9: see original paper] shows that Y distribution near the surface oxide layer is significantly affected by particle size at 0.5 vol.% oxygen content. Four powder sizes were selected: 40  $\mu\text{m}$ , 100  $\mu\text{m}$ , 190  $\mu\text{m}$ , and 300  $\mu\text{m}$ . EDS analysis of powder cross-sections revealed a distinctive feature in particles larger than 100  $\mu\text{m}$ : consistent Y peaks in line scans at the interface between the oxide layer and substrate.

**Fig. 9** Powders prepared with 0.5 vol.% oxygen in the atomizing atmosphere: (a) EDS images of 40  $\mu\text{m}$  powder, (b) EDS images of 100  $\mu\text{m}$  powder, (c) EDS images of 190  $\mu\text{m}$  powder, (d) EDS images of 300  $\mu\text{m}$  powder.

Y enrichment is closely related to powder particle size. During powder formation, migration of  $Cr^{3+}$  and  $Fe^{3+}$  within the oxide layer introduces high defect densities at the oxide-matrix interface. These defect-rich regions provide short-circuit diffusion pathways for Y atoms, promoting rapid interfacial segregation. Meanwhile, initial oxidation depletes Cr at the interface, enhancing Y chemical potential and segregation driving force in this region. Slow cooling rates for large particles provide longer diffusion times, and sufficient Y diffusion to the

interface ultimately leads to formation of a pronounced enrichment band. Additionally, rapid solidification of fine droplets forms a supersaturated Y solid solution in the matrix, which kinetically suppresses Y precipitation. In contrast, slow solidification of large droplets provides sufficient time for atoms to precipitate from the melt [?]. In summary, Y segregation is a complex process governed by synergistic effects of interface defect chemistry and solidification kinetics. Powder particle size ultimately regulates Y enrichment extent through decisive control over cooling rate and diffusion time, while defect-rich regions and elevated chemical potential induced by Cr depletion collectively provide necessary thermodynamic and kinetic preconditions for this process.

---

#### 4.4 Oxide Layer Evolution during Atomization and Solidification

Based on the above analysis, Fig. 10 [Figure 10: see original paper] illustrates oxide layer evolution during droplet solidification using atomization gas with different oxygen contents.

**Fig. 10** Evolution of the oxide layer during droplet solidification under atomization gas with different oxygen contents.

---

### 5. Conclusion

This study systematically investigated the influence of atomizing gas oxygen content on surface oxidation behaviors of ODS steel powders. The composition, thickness, and continuity of metastable oxide layers on powder surfaces can be predicted and designed by precisely controlling atomizing gas oxygen content and powder particle size. The main conclusions are:

1. Atomizing gas oxygen content is a critical factor determining oxide layer characteristics. As oxygen content increases from 0.5 to 1.0 vol.%, the oxidation mechanism changes, resulting in different oxide layer structures with correspondingly increasing overall oxide thickness.
2. Space charge theory explains the mechanism by which, under high oxygen conditions, hindered  $\text{Cr}^{3+}$  outward diffusion causes  $\text{O}^{2-}$  to migrate inward along grain boundaries and react with Fe.
3. Powder particle size, which controls cooling rate and diffusion path, causes oxide layer structure to shift from a stratified Fe-rich layer in fine powders to a mixed Fe-Cr layer in coarse powders.
4. Y is significantly segregated and enriched at the oxide layer/matrix interface of coarse powders due to slow cooling that provides sufficient time for short-circuit diffusion.

---

### **CRedit Authorship Contribution Statement**

Qian Wang: Supervision, Investigation, Funding acquisition, Conceptualization

Ji Li: Writing -original draft, Methodology, Investigation

Zijun Qi: Writing -original draft, Writing -review & editing

Bo Li: Resources

Xiaoqiang Hu: Software, Formal analysis

Hao Lan: Validation, Data curation

Yi Chen: Resources, Methodology, Funding acquisition, Conceptualization

Qi Wei: Validation, Writing -review & editing

---

### **Acknowledgment**

This work was supported by a grant from the Research Projects of Ganjiang Innovation Academy, Chinese Academy of Sciences (No. E355B0020), the 2023 Ganzhou “Jiebangguashuai” Program (2023ULGX0002), and the “Jiangxi Double Thousand Plan” (jxsq2023101058). Thanks are due to Dr. Feng and Dr. Zhu for valuable discussions.

---

### **Declaration of Competing Interest**

The authors declare that they have no known competing financial interests or personal relationships that could have appeared to influence the work reported in this paper.

---

### **Data Availability**

Data will be made available on request.

---

### **References**

- [1] H. Liu, Review on synergistic damage effect of irradiation and corrosion on reactor structural alloys. *Nucl. Tech.* (2024). 10.1007/s41365-024-01415-3
- [2] L. He, J. Li, H. Zhang et al., Effect of heat treatment on the microstructure and mechanical property of GX4CrNi13-4 manufactured by laser cladding. *Nucl. Tech.* 47, 060503 (2024). doi: 10.11889/j.0253-3219.2024.hjs.47.060503
- [3] H.E. McCoy. Status of materials development for molten salt reactors. (U.S. Department of Energy, 1978). <https://doi.org/10.2172/5195742>. Accessed 11 November 2025

- [4] H.Y. He, Y.Z. Shen, Y.J. Guo, Precipitates change of P92 steel under 3.5 MeV Fe<sup>13+</sup> irradiation 400°C. *Mater. Charact.* (2023). 10.1016/j.matchar.2023.113273
- [5] N. Baluc, R. Schäublin, P. Spätig et al., On the potentiality of using ferritic/martensitic steels as structural materials for fusion reactors. *Nucl. Fusion.* 44, 56-61 (2004). doi: 10.1088/0029-5515/44/1/006
- [6] Y.F. Chen, X.W. Wang, D. Li et al., Experimental characterization and strengthening mechanism of process-structure-property of selective laser melted 316 L. *Mater. Charact.* 198, 112753 (2023). doi: 10.1016/j.matchar.2023.112753
- [7] L.P. Xie, W.Y. Sun, J.L. Wang et al., Improving strength and oxidation resistance of a Ni-based ODS alloy via in-situ solid-state reaction. *Corros. Sci.* 197, 110078 (2022). doi: 10.1016/j.corsci.2021.110078
- [8] E. Gil, N. Ordás, C. García-Rosales et al., Microstructural characterization of ODS ferritic steels at different processing stages. *Fusion Eng. Des.* 98-99, 1973-1977 (2015). doi: 10.1016/j.fusengdes.2015.06.010
- [9] Y.L. Gu, F. Yang, Y.Y. Guo et al., Insights into the effects of oxygen content regulation on the microstructure and mechanical properties of in situ ODS 304 L stainless steel processed by laser powder bed fusion. *Nucl. Sci. Tech.* 36, 92 (2025). doi: 10.1007/s41365-025-01677-5
- [10] M.B. Wilms, S.K. Rittinghaus, M. Gossling et al., Additive manufacturing of oxide-dispersion strengthened alloys: Materials, synthesis and manufacturing. *Prog. Mater. Sci.* 133, 101049 (2023). doi: 10.1016/j.pmatsci.2022.101049
- [11] W.G. Zhai, W. Zhou, S. Nai et al., Characterization of nanoparticle mixed 316 L powder for additive manufacturing. *J. Mater. Sci. Technol.* 47, 162-168 (2020). doi: 10.1016/j.jmst.2020.02.019
- [12] H.T. Im, D.H. Kim, R.H. Kwak et al., A thermodynamic approach for preparing oxide dispersion-strengthened Ti-6Al-4V powder by in situ gas atomization method. *J. Alloys Compd.* (2024). 10.1016/j.jallcom.2023.172581
- [13] T.W. Na, K.B. Park, S.Y. Lee et al., Preparation of spherical tanbhfzrti high-entropy alloy powders by a hydrogenation-dehydrogenation reaction and thermal plasma treatment. *J. Alloys Compd.* 817, 152757 (2020). doi: 10.1016/j.jallcom.2019.152757
- [14] S.D. Gaikwad, P. Ajay, V.V. Dabhade et al., Mechanical properties and microstructural analysis of ultra-fine grained Ni-based ODS alloy processed by powder forging. *J. Alloys Compd.* (2024). 10.1016/j.jallcom.2023.172614
- [15] D. Zhang, J.T. Darsell, J. Wang et al., No ball milling needed: Alternative ODS steel manufacturing with gas atomization reaction synthesis (GARS) and friction-based processing. *J. Nucl. Mater.* (2022). 10.1016/j.jnucmat.2022.153768
- [16] J.R. Rieken, I.E. Anderson, M.J. Kramer et al., Reactive gas atomization processing for Fe-based ODS alloys. *J. Nucl. Mater.* 428, 65-75 (2012). doi: 10.1016/j.jnucmat.2011.08.015
- [17] F. Gomes, J. Barbosa, C.S. Ribeiro, Evaluation of functionally graded ceramic crucible for induction melting of TiAl based alloys. Paper Presented at the Materials 2011, (Univ Minho, Guimaraes, Portugal 18-20 April 2011).

- [18] D. Riabov, E. Hryha, M. Rashidi et al., Effect of atomization on surface oxide composition in 316L stainless steel powders for additive manufacturing. *Surf. Interface Anal.* 52, 694-706 (2020). doi: 10.1002/sia.6846
- [19] R.C. Lobb, H.E. Evans, Evaporation of elements from 20Cr-25Ni-Nb stainless-steel during vacuum annealing. *Met. Sci.* 15, 14-20 (1981). doi: 10.1179/msc.1981.15.1.14
- [20] C.F. Shi, S.Y. Chen, Q. Xia et al., Preparation and printability of 24CrNiMo alloy steel powder for selective laser melting fabricating brake disc. *Powder Metall.* 61, 73-80 (2018). doi: 10.1080/00325899.2017.1396019
- [21] S.Y. Sokovnin, V.G. Il' ves, Production of nanopowders of metal oxides using pulsed electron beam in low pressure gas. *Int. Scholarly Res. Not.* 2012, 504634 (2012). doi: 10.5402/2012/504634
- [22] Z.X. Yin, D.P. Yu, Q.B. Zhang et al., Experimental and numerical analysis of a reverse-polarity plasma torch for plasma atomization. *Plasma Chem. Plasma Process.* 41, 1471-1495 (2021). doi: 10.1007/s11090-021-10181-8
- [23] B. Lee, Gas atomization parametric study on the viga-cc based synthesis of titanium powder. *Arch. Metall. Mater.* (2020). 10.24425/amm.2020.133205
- [24] Y.K. Liu, X. Su, L.F. Fang et al., Large cryogenic magnetocaloric effect of the Laves-phase  $\text{Ho}_{1-x}\text{Dy}_x\text{Al}_2$  compounds within liquid hydrogen temperature range. *J. Alloys Compd.* 1010, 178324 (2025). doi: 10.1016/j.jallcom.2024.178324
- [25] M. Wei, S. Chen, K. Guo et al., Preparation of TA15Titanium alloy powder by EIGA for Laser 3DPrinting. *Cailiao Daobao.* 31, 64-67,78 (2017). doi: 10.11896/j.issn.1005-023X.2017.012.014
- [26] M. Xia, P. Wang, X.H. Zhang et al., Computational fluid dynamic investigation of the primary and secondary atomization of the free-fall atomizer in electrode induction melting gas atomization process. *Acta Phys. Sin.* 67, 170201 (2018). doi: 10.7498/aps.67.20180584
- [27] W.Y. Sun, M.H. Chen, Z.B. Bao et al., Breakaway oxidation of a low-Al content nanocrystalline coating at 1000°C. *Surf. Coat. Technol.* 358, 958-967 (2019). doi: 10.1016/j.surfcoat.2018.12.034
- [28] Z.M. Wang, S.G. Yang, S.B. Lawson et al., Atomic diffusivities of yttrium, titanium and oxygen calculated by Ab initio molecular dynamics in molten 316L oxide-dispersion-strengthened steel fabricated via additive manufacturing. *MATERIALS.* 17, 1543 (2024). doi: 10.3390/ma17071543
- [29] K. Dietrich, J. Diller, S. Dubiez-Le Goff et al., The influence of oxygen on the chemical composition and mechanical properties of Ti-6Al-4V during laser powder bed fusion (L-PBF). *Addit. Manuf.* 32, 100980 (2020). doi: 10.1016/j.addma.2019.100980
- [30] L. Xie, M. Chen, J. Wang et al., High temperature oxidation behavior of ultrafine grained ODS nickel-based superalloy prepared by spark plasma sintering. *J. Chin. Soc. Corros. Prot.* 42, 709-716 (2022). doi: 10.11902/1005.4537.2021.237
- [31] G. Hultquist, C. Leygraf, The initiation of selective oxidation of a ferritic stainless-steel at low-temperatures and oxygen pressures. *Corros. Sci.* 22, 331-346 (1982). doi: 10.1016/0010-938X(82)90034-8

- [32] K. Chen, Z. Liu, X. Guo et al., Effect of surface finishing on the oxidation characteristics of a Fe-21Cr-32Ni alloy in supercritical carbon dioxide. *Corros. Sci.* 195, 110019 (2022). doi: 10.1016/j.corsci.2021.110019
- [33] G. Salinas-Solano, J. Porcayo-Calderon, J.G. Gonzalez-Rodriguez et al., High temperature corrosion of inconel 600 in NaCl-KCl molten salts. *Adv. Mater. Sci. Eng.* 2014, 696081 (2014). doi: 10.1155/2014/696081
- [34] P. Deng, M. Song, J. Yang et al., On the thermal coarsening and transformation of nanoscale oxide inclusions in 316L stainless steel manufactured by laser powder bed fusion and its influence on impact toughness. *Mater. Sci. Eng. A-Struct. Mater. Prop. Microstruct. Process.* 835, 142690 (2022). doi: 10.1016/j.msea.2022.142690
- [35] Q. Zhao, Z. Qiao, J. Dong et al., Oxidation behavior analysis of a ferritic ODS steel in supercritical water. *Fusion Eng. Des.* 161, 111991 (2020). doi: 10.1016/j.fusengdes.2020.111991
- [36] I. Olefjord, L. Nyborg, Surface-analysis of gas atomized ferritic steel powder. *Powder Metall.* 28, 237-243 (1985). doi: 10.1179/pom.1985.28.4.237
- [37] J. Conceição, R. Liyanage, P.B. Armentrout, Guided ion beam studies of the reactions of  $\text{Crn}^+$  ( $n=2-14$ ) with D<sub>2</sub>: Cluster-deuteride bond energies as a chemical probe of cluster electronic structure. *Chem. Phys.* 262, 115-130 (2000). doi: 10.1016/S0301-0104(00)00162-2
- [38] B. Medasani, M.L. Sushko, K.M. Rosso et al., Vacancies and vacancy-mediated self diffusion in Cr<sub>2</sub>O<sub>3</sub>: A first-principles study. *J. Phys. Chem. C.* 121, 1817-1831 (2017). doi: 10.1021/acs.jpcc.7b00071
- [39] M. Behúlová, J. Mesárossová, P. Grgac, Analysis of the influence of the gas velocity, particle size and nucleation temperature on the thermal history and microstructure development in the tool steel during atomization. *J. Alloys Compd.* 615, S217-S223 (2014). doi: 10.1016/j.jallcom.2014.01.174
- [40] E.S. Lee, S. Ahn, Solidification progress and heat-transfer analysis of gas-atomized alloy droplets during spray forming. *Acta Metall. Mater.* 42, 3231-3243 (1994). doi: 10.1016/0956-7151(94)90421-9
- [41] E. Gil, J. Cortes, I. Iturriza et al., XPS and SEM analysis of the surface of gas atomized powder precursor of ODS ferritic steels obtained through the stars route. *Appl. Surf. Sci.* 427, 182-191 (2018). doi: 10.1016/j.apsusc.2017.07.205
- [42] M. Dejong, J. Tiarks, I. Anderson et al., Variations in GARS powder microstructure as a function of powder chemistry and particle size. *Powder Technol.* 455, 120734 (2025). doi: 10.1016/j.powtec.2025.120734
- [43] C.J. Li, W.Y. Li, Effect of sprayed powder particle size on the oxidation behavior of mcraly materials during high velocity oxygen-fuel deposition. *Surf. Coat. Technol.* 162, 31-41 (2003). doi: 10.1016/S0257-8972(02)00573-X

*Note: Figure translations are in progress. See original paper for figures.*

*Source: ChinaXiv – Machine translation. Verify with original.*